

Non-Abelian effects in dissipative photonic topological lattices

Midya Parto^{1,*}, Christian Leefmans^{2,*}, James Williams¹, Franco Nori^{3,4,5},
Alireza Marandi^{1,2,†}

¹Department of Electrical Engineering, California Institute of Technology, Pasadena, CA 91125, USA.

²Department of Applied Physics, California Institute of Technology, Pasadena, CA 91125, USA.

³Theoretical Quantum Physics Laboratory, RIKEN, Wako-shi, Saitama 351-0198, Japan.

⁴Department of Physics, University of Michigan, Ann Arbor, Michigan 48109-1040, USA.

⁵RIKEN Center for Quantum Computing, Wako, Saitama 351-0198, Japan.

*These authors contributed equally

†marandi@caltech.edu

Topology is central to phenomena that arise in a variety of fields, ranging from quantum field theory to quantum information science to condensed matter physics. Recently, the study of topology has been extended to open systems, leading to a plethora of intriguing effects such as topological lasing, exceptional surfaces, as well as the non-Hermitian bulk-boundary correspondence. Here, we show that resonator networks with dissipative couplings can be governed by matrix-valued modified Wilson lines, leading to non-Abelian effects. This is in contrast to conservative Hamiltonians exhibiting non-degenerate energy levels, where the geometric properties of the Bloch eigenstates are typically characterized by scalar Berry phases. We experimentally measure geometric phases and demonstrate non-Abelian effects in a dissipatively-coupled network of time-multiplexed photonic resonators. Our results point to new

ways in which the combined effect of topology and engineered dissipation can lead to non-Abelian topological phenomena.

According to quantum mechanics, the dynamics of a closed system is governed by a set of unitary operators. On most occasions, however, a real physical arrangement inevitably exchanges energy with its surrounding environment — something that has traditionally been considered an adverse effect, as it produces decoherence and energy decay [1]. Yet, recent studies have shown that dissipative interactions, which occur when the elements of a system exchange information through the surrounding environment, may be used as valuable tools for shaping the responses of open systems [2–4]. Such engineered dissipation has been successfully implemented in various settings, ranging from quantum computing [5, 6] and information processing [7–10] to active optical platforms to electronic and mechanical arrangements [11].

Recent years have witnessed a flurry of interest in the emerging field of topological physics [12, 13]. One of the most prominent examples of topological behavior is a set of materials exhibiting nonzero topological invariants which are endowed with an inherent robustness against local disorders [14]. This type of topological protection also occurs in physical settings beyond condensed matter physics and has led to unidirectional transport and robust features in optics [15–19], cold atoms [20, 21], mechanics [22] and acoustics [23, 24]. While topological phenomena were originally studied in closed systems, recent works on topology in *open* systems have led to a host of intriguing effects [25–30]. For instance, the interplay between topology and dissipation/gain has been utilized to develop robust and efficient coherent light sources [26, 31–36]. Other studies include the emergence of topological phases from purely dissipative interactions in the absence of Hamiltonian couplings [37–39], as well as extending the bulk-edge correspondence and topological band theory to open and non-Hermitian settings [40–45].

Gauge fields are pivotal to the understanding of topological phenomena that arise, for instance, in the Pancharatnam-Berry phases first introduced in polarization optics. Although

Abelian gauge fields have been widely used for characterizing topological states [46–50], their non-Abelian counterparts have largely remained unexplored. This is mainly due to the strict requirements, such as the existence of degenerate states in the underlying Hilbert space that are necessary in a conservative system to host non-commutative evolution operators [51, 52]. Quite recently, non-Abelian effects and topological charges have been observed in a variety of photonic systems [53–56] involving coupled waveguide arrays [57, 58] and nonreciprocal elements [59]. Despite intense research efforts in this area, studies have exclusively focused on systems with conservative couplings. In contrast, we show how the synergy between *topology* and *dissipation* can give rise to non-Abelian dynamics in the reciprocal space.

Here, we show that Lindbladians involving *dissipative couplings* can be governed by matrix-valued modified Wilson lines [51], leading to non-Abelian effects [55, 58–60]. To do so, we experimentally measure nontrivial geometric phases and demonstrate signatures of non-Abelian effects in a dissipatively-coupled network of time-multiplexed photonic resonators. In contrast to conservative systems possessing non-degenerate energy levels wherein the geometric properties of the Bloch eigenstates are typically predicted by scalar Berry phases, here, significant population exchange can occur among the ensuing dissipation bands. We illustrate these non-Abelian phenomena using example lattices in both one and two dimensions.

The general model of a Markovian open lattice is described by the Lindblad master equation:

$$\frac{d}{dt}\hat{\rho} = \mathcal{L}\hat{\rho} \equiv -i[\hat{H}, \hat{\rho}] + \sum_j \mathcal{D}[\hat{L}_j]\hat{\rho}, \quad (1)$$

where $\hat{\rho}$ represents the system density operator, \hat{H} signifies the system Hamiltonian and $\mathcal{D}[\hat{L}_j] = \hat{L}_j\hat{\rho}\hat{L}_j^\dagger - 1/2\{\hat{L}_j^\dagger\hat{L}_j, \hat{\rho}\}$ is the dissipator resulting from the nonlocal jump operators \hat{L}_j acting upon the lattice site j . When $\hat{H} = 0$, the lattice sites only exchange energy via the dissipators $\mathcal{D}[\hat{L}_j]$. Such purely dissipative couplings can be engineered to map the energy spectra of arbitrary tight-binding Hamiltonians into the decay rates of the corresponding open system [38, 61].

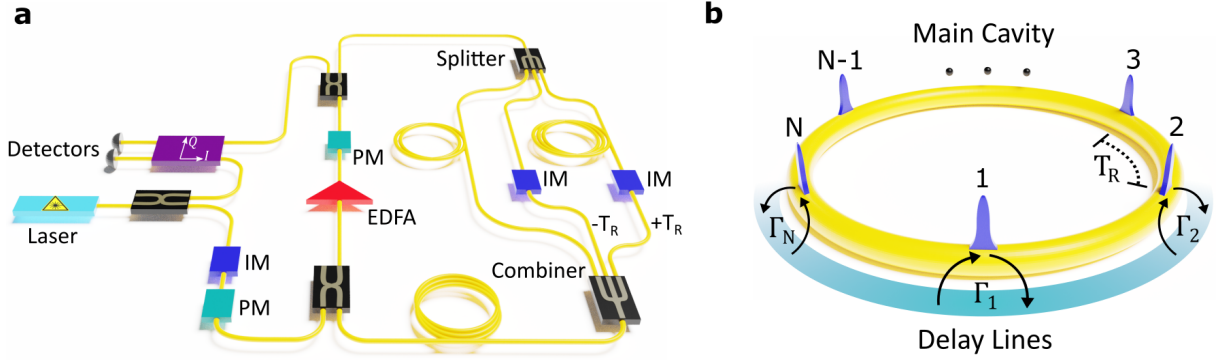


Figure 1: Network of time-multiplexed resonators. **a**, Schematic diagram of the experimental setup used to implement dissipatively coupled resonators. An intensity modulator (IM) and a phase modulator (PM) are used in the input of the optical fiber to generate arbitrary wavefunctions defined by injected femtosecond pulses from a mode-locked laser with a repetition rate of T_R . An Erbium-doped fiber amplifier (EDFA) is used in the main cavity to compensate for the losses and increase the number of measurement roundtrips. Two delay lines with smaller and larger lengths than the main cavity (corresponding to delays of $-T_R$ and $+T_R$, respectively) are used to dissipatively couple the pulses. **b**, Schematic of a resonant cavity loop (yellow) which hosts N pulses, each representing a resonator element in a dissipatively-coupled lattice. The delay lines (shown in green) provide the dissipative couplings with different rates between nearest-neighbor sites.

In particular, by properly choosing $\mathcal{D}[\hat{L}_j]$, the Lindbladian of Eq. 1 supports Bloch eigenstates characterized by bands of dissipation rates in the reciprocal space.

For our experiments, we use a time-multiplexed photonic resonator network depicted schematically in Fig. 1. This time-multiplexed network consists of a main fiber loop (the “Main Cavity”), which supports $N = 64$ resonant pulses separated by a repetition period, T_R . Each pulse represents an individual resonator associated with the annihilation (creation) operators $\hat{c}_j^{(\dagger)}$ in Eq. 1. In addition, in order to realize the jump operators \hat{L}_j , we construct delay lines to dissipatively couple the individual pulses. Each delay line is equipped with intensity modulators that control the strengths of these couplings (see Fig. 1). These delay lines can be viewed as intermediate reservoirs through which the elements of the open system exchange energy in a dissipative manner [38]. In addition, we incorporate a phase modulator in the main cavity to implement the Hamiltonian $\hat{H}_{\text{BO}} = \mathbf{F} \cdot \hat{\mathbf{r}}$, where \mathbf{F} represents a constant effective force along the lattice direction \mathbf{r} . In our experimental setup, this Hamiltonian can be approximated by a pulse-to-pulse linear phase gradient in the network.

To experimentally demonstrate Bloch oscillations (BOs), we first construct a 1D lattice with uniform, nearest-neighbor dissipative couplings (Fig. 2a). The jump operators in the master equation describing this lattice are given by $\hat{L}_j = \sqrt{\Gamma}(\hat{c}_j + \hat{c}_{j+1})$. We excite a single lattice site in the network and observe its evolution under different pulse-to-pulse phase gradients, which correspond to different BO Hamiltonians H_{BO} . We first investigate the dynamics in the absence of a phase gradient (i.e. $\hat{H}_{\text{BO}} = 0$). In this case, the excitation undergoes dissipative discrete diffraction (Fig. 2b). We emphasize that the shape of the diffraction pattern in this figure is qualitatively different from its conservative counterparts [62] due to the dissipative couplings involved. Next, we turn on the linear gradient potential associated with \hat{H}_{BO} . Figure 2c,d show experimental pulse propagation measurements associated with $\phi_0 = 2\pi/8$ and $\phi_0 = 2\pi/4$, which correspond to Bloch periods of 8 and 4 network roundtrips, respectively. As evident from

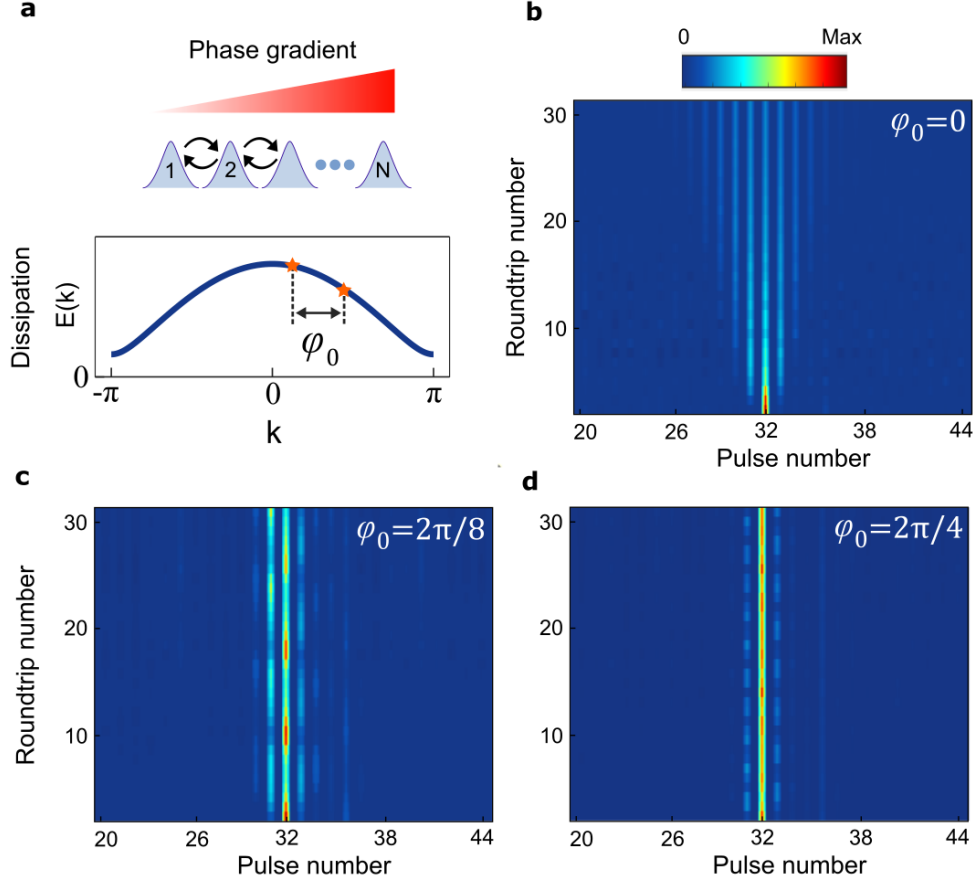


Figure 2: Experimental demonstration of Bloch oscillations in a uniform, dissipatively-coupled open lattice. **a**, Applying a phase gradient among the pulses in the time-multiplexed network transports the associated Bloch eigenstates in the reciprocal space by a value of $\delta k = \phi_0$ per cavity roundtrip, where ϕ_0 denotes the pulse-to-pulse phase differences induced by the intracavity phase modulator. **b** to **d**, Pulse intensity measurements associated with $\phi_0 = 0$, $2\pi/8$ and $2\pi/4$, respectively. In all cases, optical power is initially launched into one lattice element (pulse number 32). As shown in **(b)**, in the absence of the effective force ($\phi_0 = 0$) light undergoes dissipative discrete diffraction in the lattice. In contrast, when a nonzero phase gradient is established among the pulses, optical power exhibits an oscillatory pattern with a Bloch period equal to $N_B = 8, 4$ in **(c)**, **(d)**, respectively. In all cases, the optical power across the lattice sites is normalized in every round trip to provide a more distinct visualization of the field intensities.

these figures, the presence of pulse-to-pulse phase gradients causes the excitation to undergo periodic diffraction and refocusing, which is the hallmark of Bloch oscillations.

Typically, in a Hamiltonian lattice with multiple energy bands, the associated Bloch states tend to remain in a single band when subject to a sufficiently weak external force \mathbf{F} . Under such adiabatic conditions, the state undergoes Bloch oscillations and merely acquires a phase factor comprised of a dynamical part in addition to the geometric Berry phase associated with its energy band [63, 64]. This is in sharp contrast to Lindbladian lattices exhibiting dissipation bands which in general may not be considered in isolation. In this sense, the two-band open systems studied here exhibit reciprocal-space dynamics and band topologies similar to those of Hamiltonian systems possessing quasi-degenerate energy levels [52, 65]. Here, the reciprocal-space dynamics produced by the Lindbladian in Eq. 1, with $\hat{H} = \hat{H}_{\text{BO}}$ are governed by the modified Wilson line operator

$$\hat{W}'_{\mathbf{k}(0) \rightarrow \mathbf{k}(t)} = \mathcal{T} \exp \int dt \left[\hat{\mathbf{E}}(\mathbf{k}(t)) + i\hat{\mathbf{A}}(\mathbf{k}(t)) \cdot \mathbf{F} \right], \quad (2)$$

where \mathcal{T} indicates time ordering, $\hat{\mathbf{E}}$ is a diagonal matrix containing dissipation rates for different bands while $\hat{\mathbf{A}}$ represents the Wilczek-Zee connection matrix $\mathbf{A}_{p,q} = i \langle \phi_p(\mathbf{k}) | \nabla_{\mathbf{k}} | \psi_q(\mathbf{k}) \rangle$ at $\mathbf{k}(t) = \mathbf{k}(0) + \mathbf{F}t$ corresponding to the non-Hermitian Bloch Hamiltonian associated with the system Lindbladian [51]. Here, p, q represent two arbitrary bands of the system.

In order to show how the modified Wilson line in Eq. 2 can be used to experimentally characterize gauge fields and topological invariants within dissipative bands, we first consider a one-dimensional Su-Schrieffer-Heeger (SSH) lattice (Fig. 3a). To implement this, the intensity modulators within the network are programmed to realize the staggered couplings of the SSH model. These couplings correspond to the jump operators $\hat{L}_{A,j} = \sqrt{\Gamma_A}(\hat{c}_{A,j} + \hat{c}_{B,j})$ and $\hat{L}_{B,j} = \sqrt{\Gamma_B}(\hat{c}_{A,j+1} + \hat{c}_{B,j})$, where A and B represent the two sublattices in the structure. With these jump operators, the resulting Lindbladian exhibits a dissipative band structure that can host a

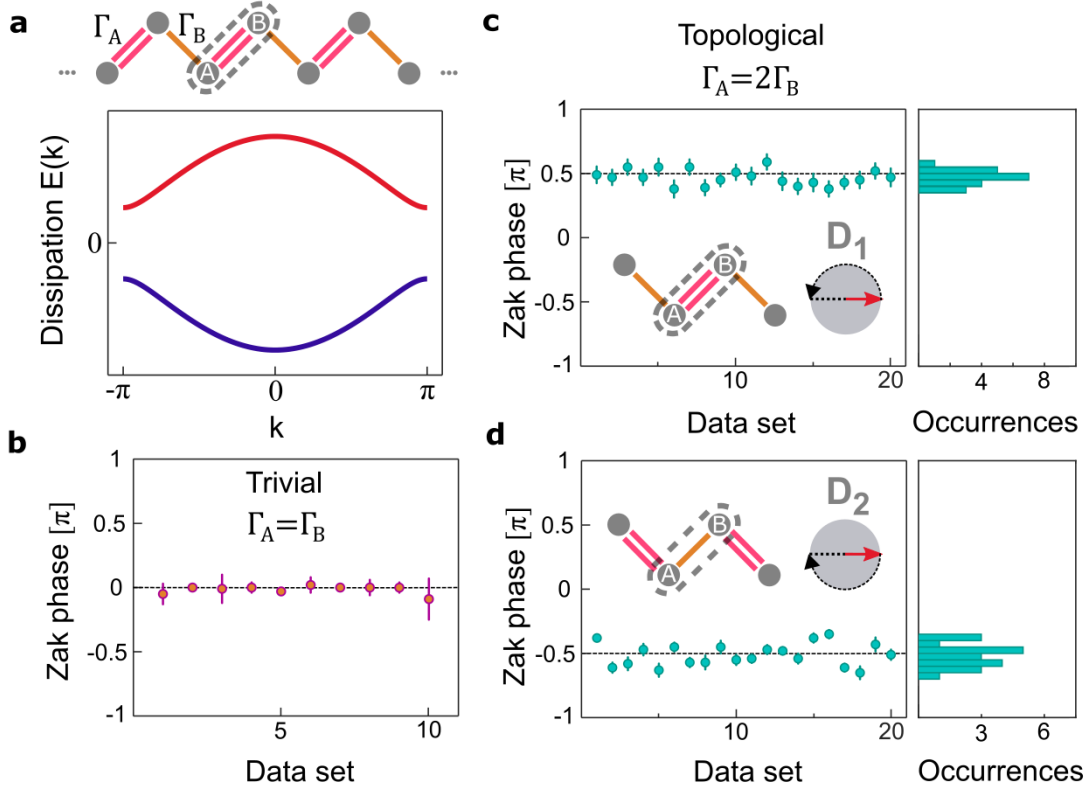


Figure 3: **Measuring the geometric Zak phase in a dissipative SSH model using dissipative Bloch oscillations.** **a**, Schematic diagram of an SSH lattice with two different couplings $\Gamma_A = 2\Gamma_B$ together with its associated dissipation bands. Since the interactions among the constituent elements are arising from the corresponding dissipators, these bands represent relative gain/decay rates, with the upper-band Bloch eigenstates experiencing relative gain while the ones associated with the lower band decay faster. **b** to **d**, Experimentally measured Zak phases under various coupling conditions. A trivial coupling between the lattice sites $\Gamma_A = \Gamma_B$ leads to a zero Zak phase (**b**). On the other hand, when the intercell and intracell dissipators differ, our measurements show $\phi_{Z1} \approx 0.47\pi$ and $\phi_{Z2} \approx -0.51\pi$ for the two possible dimerizations D_1 and D_2 shown in (**c**), (**d**), respectively. These nontrivial phases are geometrically equivalent to the counter-clockwise and clockwise windings of the upper-band Bloch eigenstates on the associated Bloch sphere, as depicted in the insets (**c**) and (**d**), respectively. Each data set represents various unit cells (shown in dashed lines) within a single measurement, except for the two first and last units to avoid edge effects.

topologically nontrivial bandgap (Fig. 3a). We first examine the upper-band geometric Berry phase θ_+ resulting from the $\mathbf{A}_{1,1}$ component of the Wilczek-Zee connection. To do so, we initially excite the upper-band Bloch eigenstate at $k = 0$. Meanwhile, the phase modulator in the cavity is programmed to impart a pulse-to-pulse phase gradient of $\phi_0 = 2\pi/8$ to initiate Bloch oscillations in the dissipatively coupled SSH lattice. After a complete Bloch period, we measure the output of the network using homodyne detection (see Fig. 1a). As expected from Eq. 2, at this point, the observed state is in a superposition of the upper- and lower-band Bloch eigenstates. Consequently, to measure the Zak phase associated with the upper band, we project the observed state into the upper-band eigenstate. Because the dissipative dynamics of our system does not impart a dynamical phase, the relative phase difference between this state and that of the originally launched pulses provides a direct measurement of the upper-band Zak phase. Figure 3b-d presents our experimentally measured values of this geometric phase in different coupling regimes of the SSH model. For $\Gamma_A = \Gamma_B$, we measure a Zak phase value of $\theta_+ = \phi_{Z0} \approx -0.02\pi$, as expected from theory (Fig. 3b). On the other hand, when $\Gamma_A \neq \Gamma_B$, our measurements show $\theta_+ = \phi_{Z1} \approx 0.47\pi$ and $\theta_+ = \phi_{Z2} \approx -0.51\pi$ for the dimerizations D_1 and D_2 depicted in Fig. 3c,d, respectively. Based on these results, the absolute value of the Zak phase in this open topological system is measured to be $\phi_Z = \phi_{Z1} - \phi_{Z2} \approx 0.98\pi$, in agreement with the theoretically expected value of $\phi_Z = \pi$ for a topologically nontrivial SSH lattice.

As discussed earlier, Eq. 2 describes different dynamics than that occurring in conservative Hamiltonian systems, since the gauge fields involved in Eq. 2 are no longer characterized by the scalar-valued Berry phases. To show this contrast, we consider a scenario wherein the Bloch eigenstate associated with the lower band of our dissipative SSH model $|\psi_-(0)\rangle$ is initially excited. Under such conditions, the off-diagonal Wilczek-Zee connections (A_{pq}) result in a nonzero population of the upper band in addition to the lower one. The effective force applied via \hat{H}_{BO} will then transport both of these eigenstates along their corresponding bands in the

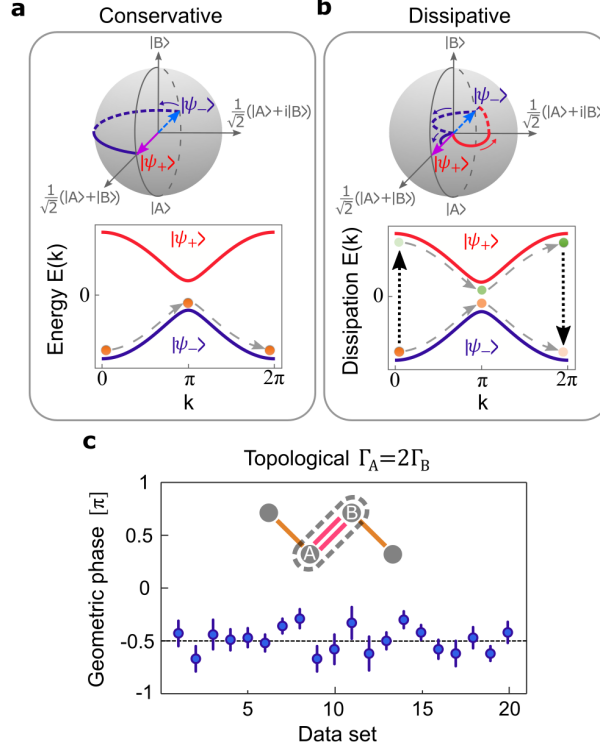


Figure 4: Modified geometric phases in the presence of non-Abelian effects. **a**, Geometric winding of the lower-band Bloch eigenstates associated with a conservative SSH Hamiltonian illustrated on the Bloch sphere. In this representation, the upper and lower Bloch eigenstates are located on the equatorial plane, shown in red and blue colors, respectively. Here, $|A\rangle$ and $|B\rangle$ represent the uniformly distributed states residing on the A and B sublattices, corresponding to the points located on the south and the north poles of the Bloch sphere, respectively. The magenta and light blue arrows represent the upper- and lower-band Bloch eigenstates associated with the Bloch momentum $k = 0$, respectively. The lower panel indicates reciprocal-space dynamics associated with the lower band, which in the adiabatic regime is independent from the upper band. **b**, Similar results for a dissipative SSH Lindbladian that are obtained from the corresponding modified Wilson line operator (Eq. 2). Unlike the conservative case (**a**), the lower-band of a dissipative SSH lattice is expected to exhibit a different geometric phase than that of the upper one. This is because the dissipation bands emerging in the latter are coupled via the off-diagonal Wilczek-Zee connections (A_{pq}), as illustrated in the lower panel of (**b**). Hence, during a Bloch period, the upper-band eigenstates (represented by green dots) are relatively amplified while those associated with the lower one (shown as orange dots) experience a higher attenuation. Eventually, the state of the system at the end of this cycle is determined by the interference between the eigenstates associated with these two bands, which is dominated by the upper-band contribution. This results in a π phase shift in the lower-band geometric phase. The left and right black dotted arrows represent the transfer of Bloch eigenstate populations from the lower band to the upper one and vice versa, respectively. **c**, Experimentally measured values (to be compared with Fig. 3 c) indeed corroborate these theoretical predictions.

reciprocal space (Fig. 4a,b). As k varies between 0 and 2π , each of the Bloch eigenstates $|\psi_{\pm}\rangle$ are multiplied by a Zak phase of $\phi_{Z1} = \pi/2$ for the D_1 configuration shown in Fig. 3c. Meanwhile, due to the dissipative nature of the bands, the upper-band eigenstate is relatively amplified while the lower one is attenuated more. Hence, at the end of the Brillouin zone when $k = 2\pi$, the contribution from the upper-band eigenstate that interferes with that associated with the lower one dominates the total population in this level due to its much higher amplitude. The combined effect of these inter-band transitions and parallel transports along the two bands of the dissipative SSH system is thus expected to impart a total phase of $\theta_- = -\pi/2$ to the original eigenstate $|\psi_-(0)\rangle$ launched in the input. We note that this behavior is in stark contrast to that expected from the SSH model implemented conservatively, where both the upper and lower bands display equal geometric phase values determined by their associated Zak phases (Fig. 4a). Figure 4c presents the experimentally measured lower-band geometric phases with a mean value of $\theta_- = -0.49\pi$, confirming our theoretical predictions based on Eq. 2.

Finally, we show how the non-Abelian nature of the modified Wilson line operator in Eq. 2 can give rise to non-commuting operators. For this purpose, we choose a dissipative honeycomb lattice as shown in Fig. 5a. Such a lattice exhibits two distinct bands of dissipation, as shown in Fig. 5b. Starting from an arbitrary Bloch momentum in the reciprocal space $\mathbf{k} = \mathbf{k}(0)$, we consider two different closed loops depicted as C_1 and C_2 in Fig. 5c. By applying a force \mathbf{F} parallel to C_i ($i = 1, 2$) an initial state $|\psi(\mathbf{k}_0)\rangle$ is transformed in the reciprocal space to a new state $\hat{\mathbf{W}}'(C_i) |\psi(\mathbf{k}_0)\rangle$. Given that these evolutions involve time-ordered integrals with matrices that in general do not commute, we expect the final state of the system to depend on the order of such operators. Figure 5d presents our simulations using Eq. 2 for two different scenarios, where the normalized initial and final states are displayed on a Bloch sphere. These results demonstrate the non-Abelian nature of the dynamics that arise in the photonic dissipative lattices considered here.

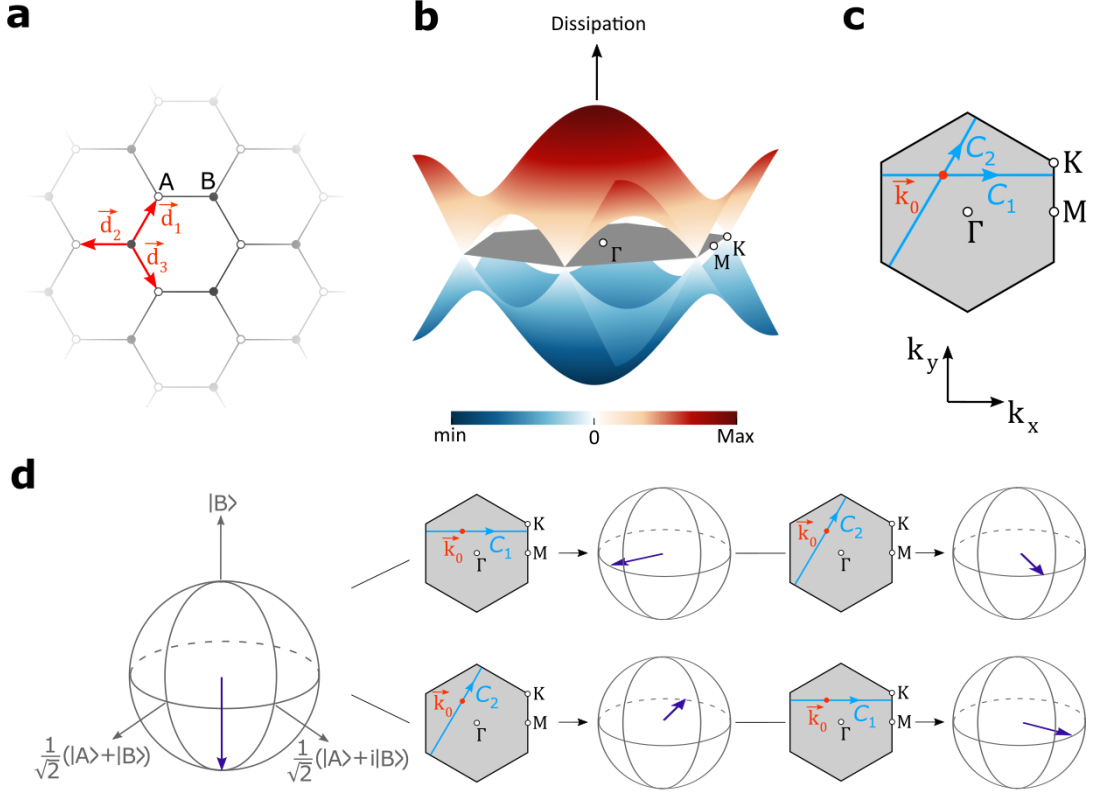


Figure 5: **Non-Abelian dynamics involving Bloch eigenstates in a dissipative honeycomb lattice.** (a) Schematic of a dissipative honeycomb lattice with two sublattices A and B . (b) Dissipation bands associated with the Bloch eigenstates of the lattice. (c) The Brillouin zone in the reciprocal space where an initial point at $\mathbf{k} = \mathbf{k}_0$ is shown together with two different closed loops C_1 and C_2 along which the initial state is transported. (d) Simulation results displaying the initial and final states on the Bloch sphere clearly show the non-commutative nature of the modified Wilson lines defined in Eq. 2, $\hat{W}'(C_1)\hat{W}'(C_2) \neq \hat{W}'(C_2)\hat{W}'(C_1)$.

In conclusion, we have shown that non-Abelian effects can arise in a dissipatively-coupled network of time-multiplexed photonic resonators. In contrast to conservative Hamiltonian systems with non-degenerate energy levels where the geometric properties are typically predicted by scalar Berry phases, here, the emerging gauge fields are in general governed by matrix-valued modified Wilson lines which may not commute for different Bloch momenta. Our measurements on the geometric Zak phases in a one-dimensional SSH model corroborates our theoretical predictions. In two dimensions, the non-Abelian nature of the underlying dynamics can be manifested in non-commutative operators acting on the Bloch eigenstates. Our findings unveil new ways in which topology and engineered dissipation can interact and lead into non-Abelian topological phenomena.

Acknowledgments

The authors acknowledge support from ARO Grant No. W911NF-18-1-0285 and NSF Grants No. 1846273 and 1918549. The authors wish to thank NTT Research for their financial and technical support.

References

1. Zurek, W. H. Decoherence, einselection, and the quantum origins of the classical. *Rev. Mod. Phys.* **75**, 715–775 (2003).
2. Poyatos, J. F., Cirac, J. I. & Zoller, P. Quantum Reservoir Engineering with Laser Cooled Trapped Ions. *Phys. Rev. Lett.* **77**, 4728–4731 (1996).
3. Diehl, S., Rico, E., Baranov, M. A. & Zoller, P. Topology by dissipation in atomic quantum wires. *Nat. Phys.* **7**, 971–977 (2011).
4. Wang, Y.-D. & Clerk, A. A. Reservoir-Engineered Entanglement in Optomechanical Systems. *Phys. Rev. Lett.* **110**, 253601 (2013).
5. Verstraete, F., Wolf, M. M. & Ignacio Cirac, J. Quantum computation and quantum-state engineering driven by dissipation. *Nat. Phys.* **5**, 633–636 (2009).

6. Gertler, J. M. *et al.* Protecting a bosonic qubit with autonomous quantum error correction. *Nature* **590**, 243–248 (2021).
7. Barreiro, J. T. *et al.* An open-system quantum simulator with trapped ions. *Nature* **470**, 486–491 (2011).
8. Shankar, S. *et al.* Autonomously stabilized entanglement between two superconducting quantum bits. *Nature* **504**, 419–422 (2013).
9. Ockeloen-Korppi, C. F. *et al.* Stabilized entanglement of massive mechanical oscillators. *Nature* **556**, 478–482 (2018).
10. Ma, R. *et al.* A dissipatively stabilized Mott insulator of photons. *Nature* **566**, 51–57 (2019).
11. El-Ganainy, R. *et al.* Non-Hermitian physics and PT symmetry. *Nat. Phys.* **14**, 11–19 (2018).
12. Hasan, M. Z. & Kane, C. L. Colloquium: Topological insulators. *Rev. Mod. Phys.* **82**, 3045–3067 (2010).
13. Qi, X.-L. & Zhang, S.-C. Topological insulators and superconductors. *Rev. Mod. Phys.* **83**, 1057–1110 (2011).
14. Thouless, D. J., Kohmoto, M., Nightingale, M. P. & den Nijs, M. Quantized Hall Conductance in a Two-Dimensional Periodic Potential. *Phys. Rev. Lett.* **49**, 405–408 (1982).
15. Rechtsman, M. C. *et al.* Photonic Floquet topological insulators. *Nature* **496**, 196–200 (2013).
16. Hafezi, M., Mittal, S., Fan, J., Migdall, A. & Taylor, J. M. Imaging topological edge states in silicon photonics. *Nat. Photon.* **7**, 1001–1005 (2013).
17. Khanikaev, A. B. *et al.* Photonic topological insulators. *Nat. Mater.* **12**, 233–239 (2013).
18. Fang, K., Yu, Z. & Fan, S. Realizing effective magnetic field for photons by controlling the phase of dynamic modulation. *Nat. Photon.* **6**, 782–787 (2012).
19. Lu, L., Joannopoulos, J. D. & Soljačić, M. Topological photonics. *Nat. Photon.* **8**, 821–829 (2014).
20. Tarruell, L., Greif, D., Uehlinger, T., Jotzu, G. & Esslinger, T. Creating, moving and merging Dirac points with a Fermi gas in a tunable honeycomb lattice. *Nature* **483**, 302–305 (2012).
21. Atala, M. *et al.* Direct measurement of the Zak phase in topological Bloch bands. *Nat. Phys.* **9**, 795–800 (2013).
22. Kane, C. L. & Lubensky, T. C. Topological boundary modes in isostatic lattices. *Nat. Phys.* **10**, 39–45 (2014).
23. Fleury, R., Khanikaev, A. B. & Alù, A. Floquet topological insulators for sound. *Nat. Commun.* **7**, 11744 (2016).

24. Yang, Z. *et al.* Topological Acoustics. *Phys. Rev. Lett.* **114**, 114301 (2015).
25. Zhou, H. *et al.* Observation of bulk Fermi arc and polarization half charge from paired exceptional points. *Science* **359**, 1009–1012 (2018).
26. Ota, Y. *et al.* Active topological photonics. *Nanophotonics* **9**, 547–567 (2020).
27. Bergholtz, E. J., Budich, J. C. & Kunst, F. K. Exceptional topology of non-Hermitian systems. *Rev. Mod. Phys.* **93**, 015005 (2021).
28. Ashida, Y., Gong, Z. & Ueda, M. Non-Hermitian physics. *Adv. Phys.* **69**, 249–435 (2020).
29. Xia, S. *et al.* Nonlinear tuning of PT symmetry and non-Hermitian topological states. *Science* **372**, 72–76 (2021).
30. Weidemann, S., Kremer, M., Longhi, S. & Szameit, A. Topological triple phase transition in non-Hermitian Floquet quasicrystals. *Nature* **601**, 354–359 (2022).
31. Bandres, M. A. *et al.* Topological insulator laser: Experiments. *Science* **359**, eaar4005 (2018).
32. Bahari, B. *et al.* Nonreciprocal lasing in topological cavities of arbitrary geometries. *Science* **358**, 636–640 (2017).
33. Zeng, Y. *et al.* Electrically pumped topological laser with valley edge modes. *Nature* **578**, 246–250 (2020).
34. St-Jean, P. *et al.* Lasing in topological edge states of a one-dimensional lattice. *Nat. Photon.* **11**, 651–656 (2017).
35. Parto, M. *et al.* Edge-Mode Lasing in 1D Topological Active Arrays. *Phys. Rev. Lett.* **120**, 113901 (2018).
36. Zhao, H. *et al.* Topological hybrid silicon microlasers. *Nat. Commun.* **9**, 981 (2018).
37. Bardyn, C.-E. *et al.* Topology by dissipation. *New J. Phys.* **15**, 085001 (2013).
38. Leefmans, C. *et al.* Topological dissipation in a time-multiplexed photonic resonator network. *Nature Physics* **18**, 442–449 (2022).
39. Yoshida, T. & Hatsugai, Y. Bulk-edge correspondence of classical diffusion phenomena. *Sci. Rep.* **11**, 888 (2021).
40. Kunst, F. K., Edvardsson, E., Budich, J. C. & Bergholtz, E. J. Biorthogonal Bulk-Boundary Correspondence in Non-Hermitian Systems. *Phys. Rev. Lett.* **121**, 026808 (2018).
41. Gong, Z. *et al.* Topological Phases of Non-Hermitian Systems. *Phys. Rev. X* **8**, 031079 (2018).
42. Yao, S. & Wang, Z. Edge States and Topological Invariants of Non-Hermitian Systems. *Phys. Rev. Lett.* **121**, 086803 (2018).
43. Xiao, L. *et al.* Non-Hermitian bulk–boundary correspondence in quantum dynamics. *Nat. Phys.* **16**, 761–766 (2020).

44. Weidemann, S. *et al.* Topological funneling of light. *Science* **368**, 311–314 (2020).
45. Helbig, T. *et al.* Generalized bulk–boundary correspondence in non-Hermitian topoelectrical circuits. *Nat. Phys.* **16**, 747–750 (2020).
46. Hafezi, M. Measuring Topological Invariants in Photonic Systems. *Phys. Rev. Lett.* **112**, 210405 (2014).
47. Hu, W. *et al.* Measurement of a Topological Edge Invariant in a Microwave Network. *Phys. Rev. X* **5**, 011012 (2015).
48. Wimmer, M., Price, H. M., Carusotto, I. & Peschel, U. Experimental measurement of the Berry curvature from anomalous transport. *Nat. Phys.* **13**, 545–550 (2017).
49. Wang, K. *et al.* Generating arbitrary topological windings of a non-Hermitian band. *Science* **371**, 1240–1245 (2021).
50. Wang, K., Dutt, A., Wojcik, C. C. & Fan, S. Topological complex-energy braiding of non-Hermitian bands. *Nature* **598**, 59–64 (2021).
51. Wilczek, F. & Zee, A. Appearance of Gauge Structure in Simple Dynamical Systems. *Phys. Rev. Lett.* **52**, 2111–2114 (1984).
52. Culcer, D., Yao, Y. & Niu, Q. Coherent wave-packet evolution in coupled bands. *Physical Review B* **72**, 085110 (2005).
53. Xu, J.-S. *et al.* Simulating the exchange of Majorana zero modes with a photonic system. *Nature Communications* **7**, 13194 (2016).
54. Ma, L. B. *et al.* Spin–orbit coupling of light in asymmetric microcavities. *Nature Communications* **7**, 10983 (2016).
55. Chen, Y. *et al.* Non-Abelian gauge field optics. *Nature Communications* **10**, 3125 (2019).
56. Guo, Q. *et al.* Experimental observation of non-Abelian topological charges and edge states. *Nature* **594**, 195–200 (2021).
57. Noh, J. *et al.* Braiding photonic topological zero modes. *Nature Physics* **16**, 989–993 (2020).
58. Zhang, X.-L. *et al.* Non-Abelian braiding on photonic chips. *Nature Photonics*, 1–6 (2022).
59. Yang, Y. *et al.* Synthesis and observation of non-Abelian gauge fields in real space. *Science* **365**, 1021–1025 (2019).
60. Iadecola, T., Schuster, T. & Chamon, C. Non-Abelian Braiding of Light. *Physical Review Letters* **117**, 073901 (2016).
61. Wanjura, C. C., Brunelli, M. & Nunnenkamp, A. Topological framework for directional amplification in driven-dissipative cavity arrays. *Nat. Commun.* **11**, 3149 (2020).
62. Christodoulides, D. N., Lederer, F. & Silberberg, Y. Discretizing light behaviour in linear and nonlinear waveguide lattices. *Nature* **424**, 817–823 (2003).

- 63. Wilkinson, S. R. *et al.* Experimental evidence for non-exponential decay in quantum tunnelling. *Nature* **387**, 575–577 (1997).
- 64. Shevchenko, S. N., Ashhab, S. & Nori, F. Landau–Zener–Stückelberg interferometry. *Phys. Rep.* **492**, 1–30 (2010).
- 65. Li, T. *et al.* Bloch state tomography using Wilson lines. *Science* **352**, 1094–1097 (2016).